

Viscoacoustic waveform inversion of velocity structures in the time domain

Jianyong Bai¹, David Yingst¹, Robert Bloor², and Jacques Leveille¹

ABSTRACT

Because of the conversion of elastic energy into heat, seismic waves are attenuated and dispersed as they propagate. The attenuation effects can reduce the resolution of velocity models obtained from waveform inversion or even cause the inversion to produce incorrect results. Using a viscoacoustic model consisting of a single standard linear solid, we discovered a theoretical framework of viscoacoustic waveform inversion in the time domain for velocity estimation. We derived and found the viscoacoustic wave equations for forward modeling and their adjoint to compensate for the attenuation effects in viscoacoustic waveform inversion. The wave equations were numerically solved by high-order finite-difference methods on centered grids to extrapolate seismic wavefields. The finite-difference methods were implemented satisfying stability conditions,

which are also presented. Numerical examples proved that the forward viscoacoustic wave equation can simulate attenuative behaviors very well in amplitude attenuation and phase dispersion. We tested acoustic and viscoacoustic waveform inversions with a modified Marmousi model and a 3D field data set from the deep-water Gulf of Mexico for comparison. The tests with the modified Marmousi model illustrated that the seismic attenuation can have large effects on waveform inversion and that choosing the most suitable inversion method was important to obtain the best inversion results for a specific seismic data volume. The tests with the field data set indicated that the inverted velocity models determined from the acoustic and viscoacoustic inversions were helpful to improve images and offset gathers obtained from migration. Compared to the acoustic inversion, viscoacoustic inversion is a realistic approach for real earth materials because the attenuation effects are compensated.

INTRODUCTION

Waveform inversion is the name given to a set of techniques that seek to estimate subsurface parameters by minimizing the difference or residuals between recorded and synthetic seismic data produced with a specific set of subsurface parameters and forward modeling equations. The difference to be minimized is constructed using a specific choice of norm, which will be discussed later. Waveform inversion is attractive because it has the ability to produce high-resolution subsurface parameter models for complex geologic structures (Virieux and Operto, 2009). Lailly (1983), Tarantola (1984, 1987, 1988), and Mora (1987, 1988) introduce the gradient-based waveform inversion in the time domain with its increased efficiency and reduced computational cost. Their methods

make applications possible for data sets of sizes used in exploration and production; since then, many researchers have achieved substantial improvements in theory and application. Today, waveform inversion has become a practical if not quite yet routine tool for field-scale exploration and production applications (Sirgue et al., 2009; Prioux et al., 2011; Vigh et al., 2011). An excellent and comprehensive review of waveform inversion techniques and applications has been given by Virieux and Operto (2009).

Waveform inversion is an iterative optimization technique, where each step in the iteration produces a model update. Each update must calculate the gradient of the objective function with respect to the model parameters (Tarantola, 1987, 1988; Virieux and Operto, 2009). There are three key steps for the calculation of the gradient in waveform inversion. The first step is the calculation

Manuscript received by the Editor 23 January 2013; revised manuscript received 16 December 2013; published online 2 May 2014.

¹ION Geophysical Corporation, CityWest Boulevard, Houston, Texas, USA. E-mail: jianyong.bai@iongeo.com; david.yingst@iongeo.com; jacques.leville@iongeo.com.

²Formerly ION Geophysical Corporation, CityWest Boulevard, Houston, Texas, USA; presently Schlumberger, San Felipe, Houston, Texas, USA. E-mail: rbloor@slb.com.

© 2014 Society of Exploration Geophysicists. All rights reserved.

of residuals between the recorded and synthetic seismic data. The synthetic seismic data are obtained through forward modeling, i.e., the calculation of seismic wavefields at given positions and times by solving appropriate wave equations with boundary conditions and with a chosen set of subsurface parameters. The second step is the backward propagation of the residuals based on the adjoint-state method (Tarantola, 1987, 1988; Bunks et al., 1995; Plessix, 2006). The residuals are backward propagated through the adjoint of forward modeling. Numerical methods such as the finite-difference, finite-element, finite-volume, and spectral-element methods are widely used to solve a wave equation and its adjoint (Virieux and Operto, 2009). The third and final step is the calculation of the gradient through the crosscorrelation of forward and backward wavefields at each time step and a summation of the crosscorrelation over all time steps. The gradient indicates the descent directions within the parameter space to update the current model.

The adjoint-state method is thoroughly explained in the paper of Plessix (2006), which takes a well-known technique of numerical optimization to the geophysical community. Basically, the problem that we are trying to solve is an optimization in functional space, where the functional that we are trying to minimize is a function of the model parameters and the wavefields (the state variables) that we have computed using specific wave equations and boundary conditions. The wavefields are themselves functionals of the model parameters. So to compute the gradient of the functional, we should, in principle, calculate the Fréchet derivatives, i.e., the derivatives of the state variables (the calculated wavefields) with respect to the model parameters. The Fréchet derivatives are themselves extremely expensive to calculate and must be done multiple times per iteration. With the adjoint state method, one expands the “Lagrangian,” i.e., the functional to be minimized using Lagrange multipliers that force the wavefields to satisfy the appropriate wave equations and boundary conditions. The augmented Lagrangian contains a term that includes the inner product of the Lagrange multipliers (the adjoint-state variables) and the wave-equation constraint. By exploiting the definition of the adjoint operator, one can rewrite this term as the adjoint operator acting on the adjoint variables, so that the variations over the state variables now become another wave equation (which is acausal) with the residual as sources. The variation of the Lagrangian with respect to the model parameters then yields the gradient as a crosscorrelation of the adjoint-state variable determined through the forward problem and as a simple function of the state variables. Because the adjoint state equation only needs to be solved once per iteration rather than the multiple times that the Fréchet derivative need to be computed (once for each small perturbation of the model), this minimizes computational cost substantially. Plessix describes many applications such as least-squares migration (Lailly, 1983; Tarantola, 1984), differential semblance optimization (Symes and Carazzone, 1991; Shen et al., 2003) and stereotomography (Billette and Lambaré, 1998). For a very lucid application specific to full-waveform inversion, see Bunks et al. (1995). This is very much in the line with the teachings of Tarantola (1988; p. 366) who instructs us that “. . . methods of inversion based on naïve use of least-squares formulas do not work. In particular, matrix algebra must not be used and partial (or Fréchet) derivatives of data with respect to model parameters should not be computed.”

The quality of waveform inversion critically depends on the adequacy of the forward-modeling wave equation and of its adjoint

to correctly represent the physics for all the waves that we observe in nature, namely in our data sets (Tarantola, 1988), not only in the continuous domain but also with their discretized approximations (Bunks et al., 1995). Here, the wave equations play a crucial role because the complete and accurate solutions of a wave equation and its adjoint ensure that wavefields provide useful information to improve parameter models. Depending on the characteristics of the physical medium, various approximations are made and thus different wave equations might be applied. The acoustic wave equation is applied for acoustic and isotropic media either in the time domain (Mora, 1987; Bunks et al., 1995; Shipp and Singh, 2002; Vigh and Starr, 2008) or in the frequency domain (Pratt and Worthington, 1990; Pratt, 1999; Sirgue and Pratt, 2004; Shin and Min, 2006; Operto et al., 2007; Yingst et al., 2011). Anisotropic wave equations are applied for anisotropic media to improve model construction (Operto et al., 2009; Lee et al., 2010; Plessix and Rynja, 2010; Gholami et al., 2011, 2012; Wang et al., 2012), and elastic wave equations are applied for the more general elastic case to obtain more accurate information of subsurface media (Tarantola, 1986, 1988; Sears et al., 2010; Oh et al., 2012). The acoustic or elastic wave equations are adequate to describe wave propagation in lossless media and are a good choice to solve a lot of practical problems.

However, wave propagation in real earth materials is quite different from propagation in an ideal acoustic or elastic medium. The real earth always attenuates and disperses seismic waves due to the conversion of elastic energy into heat. This anelastic behavior can decrease amplitude, distort a wavelet, and thus can have significant effects on waveform inversion. For example, gas clouds can cause strong attenuation of compressional seismic waves. The attenuation effects result in the loss of high frequencies in the recorded data and result in the amplitude below the gas clouds to be anomalously dim. As a result, gas clouds can cause serious discrepancies between the recorded and synthetic seismic data, and thus reduce the resolution of inversion results or invalidate the results. Gas clouds are only one example of attenuation of propagating seismic waves within real earth materials. They indicate that when the attenuation cannot be ignored, it is necessary to compensate for the anelastic behavior to make inversion results more reliable for physical media.

Various models are commonly used to compensate for the anelastic effects in seismology and seismic data processing (Toksöz and Johnston, 1981). The attenuation coefficient is proportional to frequency in the Kolsky-Futterman model (Kolsky, 1956; Futterman, 1962). A constant- Q model (Kjartansson, 1993) is also often used in the frequency domain (Liao and McMechan, 1996). The standard linear solid (SLS) model is used in finite-difference methods because it gives additional differential equations that are able to be approximated by finite differences (Carcione, 1993; Robertsson et al., 1994).

A viscoelastic mechanical model consisting of SLS models provides a powerful tool to model real earth materials through relaxation mechanism (Liu et al., 1976; Day and Minster, 1984; Carcione, 1993; Robertsson et al., 1994). A single SLS consists of a spring in parallel with a spring and a dashpot in series. It is able to provide a good approximation to a constant Q within a defined frequency band. A series of SLS models connected in parallel can yield a quite general mechanical viscoelasticity behavior. In an SLS, the stress-strain relationship is expressed as a causal time convolution of a stress relaxation function with the strain rate. This time

dependence of relaxation mechanism is governed by stress and strain relaxation times, which describe the physical dissipation mechanism that the real earth materials have on wave propagation. [Carcione \(2001\)](#) presents the relationships between the quality factor Q and the relaxation times in a given frequency band. [Blanch et al. \(1995\)](#) estimate the relaxation times from the least-squares fitting of Q^{-1} over a frequency range. Finite-difference wavefield computations implemented on staggered grids have shown that the SLSs model can simulate realistic wave propagation well in earth materials ([Carcione, 1993](#); [Robertsson et al., 1994](#); [Larsen and Grieger, 1998](#)).

In his remarkable paper, [Tarantola \(1988\)](#) set out a very general framework for wave equations for the description of elasticity and attenuation in realistic earth materials in the time domain. Although the paper is highly theoretical and does not apply the theory to synthetics and/or real data examples, it sets out a method for the forward problem and the inverse problem through the transpose and adjoint methods. The attenuation is described by producing a generalized Hooke's law whereby the stresses are related to the strains via a convolution with the rate of relaxation function that is quite general and can also handle anisotropy in elasticity and attenuation.

We must emphasize that several other authors have applied waveform inversion with attenuation for P-wave velocity (V_p) and Q , mostly in 2D or 2.5D in the frequency domain (see the review of [Virieux and Operto, 2009](#)). V_p and Q are inverted either recursively or simultaneously ([Kamei and Pratt, 2013](#)). In a recursive method, one parameter is inverted with another parameter fixed ([Smithyman and Clowes, 2013](#)). A specific example is presented by [Malinowski et al. \(2011\)](#) who applied waveform inversion in the frequency domain to a 2D land data set in Poland. Their parameterization of attenuation is using a complex velocity representation. They invert for velocity and Q simultaneously, after carefully studying the resolution that this joint inversion provides. [Kamei and Pratt \(2013\)](#) also present an approach of simultaneous inversion in the frequency domain by using an attenuation scaling term in their preconditioning operator.

In this paper, we limit our work to viscoacoustic media. We set up an objective function and derive a normalized gradient for velocity update through viscoacoustic waveform inversion in the time domain. According to the relaxation mechanism in a single SLS, we derive the viscoacoustic wave equations for forward modeling and their adjoint. Compared to the acoustic wave equation, the viscoacoustic wave equations and their adjoint involve a time convolution for the relaxation mechanism. The convolutions are expressed as memory variables and are responsible for attenuation. The forward operator simulates the attenuation effects and, in contrast, its adjoint compensates for the attenuation effects. This compensation for the attenuation of the adjoint was already explained by [Tarantola \(1988\)](#), where he notes that the general adjoint equation would be acausal, i.e., propagating backward in time and with "negative attenuation" but still be numerically stable. We implement the viscoacoustic waveform inversion by high-order finite-difference methods on centered grids. The stability requirement for hyperbolic differential equations on centered grids is given through a Von Neumann stability analysis.

Our formulation of waveform inversion in this paper follows very much the lines of the [Tarantola's \(1988\)](#) paper, where we specialize to an acoustic approximation and where the rate of relaxation function is that for a single SLS that describes the attenuation through

the standard variable parameter Q . We rederive the acoustic equations and their adjoints as well. However, the generalization to a more complex model of attenuation is straightforward, but not attempted in this paper.

Viscoacoustic forward modeling examples demonstrate that reasonable attenuative behaviors in amplitude attenuation and phase dispersion can be obtained from our viscoacoustic wave equations. We apply acoustic and viscoacoustic waveform inversions on a modified Marmousi model and a 3D field data set from the Gulf of Mexico (GOM). The tests clearly show some promise in making waveform inversion more realistic for real earth materials. It is noted that we employ a recursive procedure, where we first update the velocity through several iterations of waveform inversion, then we update the Q model. Having obtained a stable Q model we then iterate through a velocity inversion step. Again, this is very much in line with the advice of [Tarantola \(1988, p. 388\)](#), to "first invert for elastic parameters, and, after convergence, allow attenuation to be introduced."

This paper is laid out as follows: In the next section, we set out the theory deriving the forward and adjoint wave equations for an attenuation model based on a single SLS. We then follow with a section showing results on synthetic data and a 3D GOM field data set.

THEORY

Objective function

We iteratively optimize a velocity model by minimizing the following objective function, which measures the residuals between the recorded and synthetic seismic data:

$$J(v) = \|d_0 - \alpha d\|_2^2, \quad (1)$$

where $d_0 = d_0(\mathbf{x}_r, t; \mathbf{x}_s)$ is the recorded seismic data; $d = d(\mathbf{x}_r, t; \mathbf{x}_s)$ is the synthetic seismic data at time t and at the receiver located at \mathbf{x}_r for a source located at \mathbf{x}_s ; and $\alpha = \langle d, d_0 \rangle / \|d\|^2$ is a normalization scale. In practice, the energy level of the synthetic data is generally different from that of the recorded data. The different energy levels between them can cause failure of waveform inversion. The normalization helps to mitigate this problem. It is noted that the normalization within the objective function is a single constant for all traces and all times within one shot. As a result, amplitude variations are involved in waveform inversion.

In the objective function, different preconditioning methods can be applied to the recorded and synthetic data to improve convergence and to mitigate the nonlinearity of the inverse problem. [Bunks et al. \(1995\)](#) present the multiscale strategy of inverting low frequencies first and progressively inverting higher frequencies. [Sears et al. \(2008\)](#) and [Brossier et al. \(2009\)](#) demonstrate that windowing the early arrivals or tapering the late arrivals is helpful to improve the convergence to the global minimum. [Shipp and Singh \(2002\)](#) indicate that weighting far-offset data is helpful to strengthen the contribution of large-offset data for the convergence toward acceptable velocity models.

The gradient for velocity update is given by

$$g(\mathbf{x}) = -\frac{4\alpha}{v^3} \sum_{\mathbf{x}_s} \sum_t \frac{\partial^2 P}{\partial t^2} R, \quad (2)$$

where $P = P(\mathbf{x}, t; \mathbf{x}_s)$ is the predicted wavefield obtained from a forward modeling operator and $R = R(\mathbf{x}, t; \mathbf{x}_s)$ is the wavefield obtained by applying the adjoint of forward modeling on the residual $(d_0 - \alpha d)$. The relationship between d and P is $d(\mathbf{x}, t; \mathbf{x}_s) = P(\mathbf{x}, t; \mathbf{x}_s)|_{\mathbf{x}=\mathbf{x}_s}$.

Some preconditioning methods can also be applied to the gradient to improve the convergence and to mitigate the nonlinearity of the inverse problem, for example, smoothing and/or filtering the gradient in the wavenumber domain (Nemeth et al., 1997; Guitton et al., 2012; Ma et al., 2012) and using depth-dependent weights for the gradient (Shipp and Singh, 2002; Wang and Rao, 2009). Moreover, the gradient can be normalized by the amplitude of the forward wavefield to approximately account for geometrical divergence (Gauthier et al., 1986)

$$g_n(\mathbf{x}) = \frac{g(\mathbf{x})}{\sqrt{\sum_{\mathbf{x}_s} \sum_t P^2(\mathbf{x}, t; \mathbf{x}_s) + \gamma^2}}, \quad (3)$$

where γ is a whitening factor to avoid any singularity.

The velocity model is updated using the Polak-Ribière implementation of nonlinear conjugate gradient method. A line search uses the BB formula (Barzilai and Borwein, 1988) for an initial estimate of step length. The BB formula effectively provides an initial guess of the step length for the nonlinear problem because it does not require extra forward modeling to evaluate the objective function (Li, 2011).

Viscoacoustic wave equation

In viscoacoustic media, the predicted wavefield can be obtained by the relationship between pressure and particle velocity for a single SLS (Robertsson et al., 1994):

$$\frac{\partial P}{\partial t} = - \frac{\partial \left[\kappa \left(1 + \tau e^{-\frac{t}{\tau}} \right) H(t) \right]}{\partial t} * \nabla \cdot \mathbf{v} + f \quad (4)$$

and

$$\frac{\partial \mathbf{v}}{\partial t} = - \frac{1}{\rho} \nabla P, \quad (5)$$

where $\rho = \rho(\mathbf{x})$ is the density at the position \mathbf{x} , $\kappa = \kappa(\mathbf{x})$ is the bulk modulus, $\mathbf{v} = \mathbf{v}(\mathbf{x}, t)$ is the particle velocity vector, $f = f(\mathbf{x}_s, t)$ is the source term at \mathbf{x}_s , and $H(t)$ is the Heaviside function. The symbol $*$ stands for a time convolution in equation 4. The convolution describes the dissipation mechanism in a viscoacoustic medium. Here, τ_σ and τ_ϵ are, respectively, stress and strain relaxation times, and $\tau = \tau_\epsilon / \tau_\sigma - 1$ determines the magnitude of Q (Liu et al., 1976). By choosing the center of frequency band for waveform inversion as the reference frequency, the relaxation times can be calculated from the quality factor Q according to the methods presented by Carcione (2001) or Blanch et al. (1995). Finite-difference methods on staggered grids are commonly used to extrapolate the wavefield P based on equations 4 and 5 (Carcione, 1993; Robertsson et al., 1994).

We start from equations 4 and 5 and derive the following viscoacoustic wave equation (see Appendix A) for forward modeling:

$$\frac{1}{v^2} \frac{\partial^2 P}{\partial t^2} = (1 + \tau) \rho \nabla \cdot \left(\frac{1}{\rho} \nabla P \right) - r + f \quad (6)$$

with

$$r = \frac{\tau}{\tau_\sigma} \left[e^{-\frac{t}{\tau_\sigma}} H(t) \right] * \left[\rho \nabla \cdot \left(\frac{1}{\rho} \nabla P \right) \right], \quad (7)$$

where r is a memory variable. Equation 6 describes combined acoustic and viscous behavior of a material. It indicates that the second-order derivative of pressure with respect to time depends on the values obtained from $\rho \nabla \cdot ((1/\rho) \nabla P)$ and their history.

The memory variable r is governed by a time convolution of $\rho \nabla \cdot ((1/\rho) \nabla P)$ with an exponential function; i.e., the kernel of r is of exponential character. Here, the exponential function is the relaxation function. Because r decays with time, energy is dissipated. This procedure simulates the attenuation effects in forward modeling.

To eliminate the convolution in equation 7, we derive the first-order linear differential equation for r and update it by a recursive convolution method (see Appendix A):

$$\frac{\partial r}{\partial t} = \frac{\tau}{\tau_\sigma} \rho \nabla \cdot \left(\frac{1}{\rho} \nabla P \right) - \frac{1}{\tau_\sigma} r. \quad (8)$$

Adjoint operator

According to the adjoint-state method (Tarantola, 1987, 1988; Plessix, 2006), the adjoint of forward modeling is required for the calculation of gradient. The adjoint backward propagates the residuals between the recorded and synthetic seismic data by reducing time. Based on the properties of the adjoint of an operator, we can verify that the adjoint operator solves the following equation (see Appendix B):

$$\frac{1}{v^2} \frac{\partial^2 P}{\partial t^2} = \nabla \cdot \frac{1}{\rho} \nabla (1 + \tau) \rho P - \nabla \cdot \frac{1}{\rho} \nabla \rho \tilde{r} + f \quad (9)$$

with

$$\tilde{r} = \frac{\tau}{\tau_\sigma} \left[e^{\frac{t}{\tau_\sigma}} H(-t) \right] * P, \quad (10)$$

where f is the residual $(d_0 - \alpha d)$, and the memory variable \tilde{r} is the history of pressure and is responsible for the anelastic behavior. The \tilde{r} is governed by a time convolution of pressure with an exponential function. Here, the exponential function is the relaxation function. The kernel of \tilde{r} is of exponential character too. Energy now increases with decreasing time in the backward propagation.

Similarly, we derive the first-order linear differential equation for \tilde{r} and update it by a recursive convolution method (see Appendix B):

$$\frac{\partial \tilde{r}}{\partial t} = - \frac{\tau}{\tau_\sigma} P + \frac{1}{\tau_\sigma} \tilde{r}. \quad (11)$$

Equations 6, 8, 9, and 11 present all operators for wavefield extrapolation in viscoacoustic waveform inversion to compensate

for the attenuation effects in a viscoacoustic medium. We calculate the memory variables r and \tilde{r} on the same grids used for the waveform P. As a result, the viscoacoustic waveform inversion is able to be implemented by high-order finite-difference methods on centered grids.

Stability conditions

Finite-difference solutions introduce numerical dispersion due to the time and space discretization. The numerical dispersion originates from two sources in viscoacoustic waveform inversion. The first source of these numerical artifacts is introduced in the second-order differential equations 6 and 7 governing the forward and backward wave propagation. A second type of dispersion is the unwanted dispersion from the first-order differential equations 8 and 9 governing the memory variables. We must therefore determine the spatial and temporal sampling criteria and restrictions to avoid or minimize these numerical dispersion effects.

The rule of thumb in finite-difference schemes for choosing the spatial sampling rate Δx based on the Nyquist frequency f_N is $\Delta x = v_{\min}/(n \times f_N)$, where v_{\min} is the minimum velocity in the velocity cube, and n is the number of points needed to cover the Nyquist frequency for nondispersive propagation. The value of n is scheme dependent. Throughout the paper, we use the $O(m, n)$ notation to describe the accuracy of the finite-difference schemes for m th-order accuracy in time and n th-order accuracy in space. According to Dablain (1986), $n = 8$ for $O(2, 2)$, $n = 4$ for $O(2, 4)$, and $n = 3$ for $O(4, 10)$.

Following the method originally developed by Von Neumann for the stability analysis of finite-difference solutions (Charney et al., 1950), the temporal sampling for the hyperbolic differential wave equations 6 and 9 is chosen to be

$$\Delta t \leq \frac{2}{v_{\max} \sqrt{a(1 + \tau_{\max})}} \quad (12)$$

with

$$a = \frac{1}{\Delta x^2} \sum_{n=-N}^N |w_n^x| + \frac{1}{\Delta y^2} \sum_{n=-N}^N |w_n^y| + \sum_{n=-N}^N \frac{|w_n^z|}{\Delta z^2}, \quad (13)$$

where v_{\max} is the maximum velocity in the velocity cube; τ_{\max} is the maximum value of the τ cube; Δt is the temporal step size; Δx , Δy , and Δz are the spatial sampling intervals along the x -, y -, and z -axes, respectively; and w values are finite-differencing coefficients in the x -, y -, and z -directions with $(2N)$ th-order accuracy (Dablain, 1986). To reduce computation cost, the interval Δz can be nonuniform.

Unless otherwise specified for the examples in this paper, we employ the $O(2, 8)$ scheme for the second-order differential equations 6 and 9 and employ the second-order Crank-Nicolson scheme (Crank and Nicolson, 1947) in time and the eighth-order centered difference in space for the first-order differential equations 8 and 11. The Crank-Nicolson scheme proves to be adequate for stability and accuracy with a temporal step size that satisfies the criterion 11. In these finite-difference schemes, Higdon's second-order absorbing boundary condition is applied (Higdon, 1991).

EXAMPLES

Step structure

We use a 3D numerical example to illustrate the simulation of attenuation effects by using the viscoacoustic wave equation 6. Carcione et al. (1988b) and Blanch et al. (1995) show that wave equations with different number of SLSs, including a single SLS approximation, can reproduce analytical solutions with reasonable accuracy. In this numerical example, we will benchmark equation 6 against equation 4.

Assuming a constant density $\rho = 1 \text{ g/cm}^3$ and a constant velocity ($v = 1500 \text{ m/s}$), let us consider a heterogeneous Q model

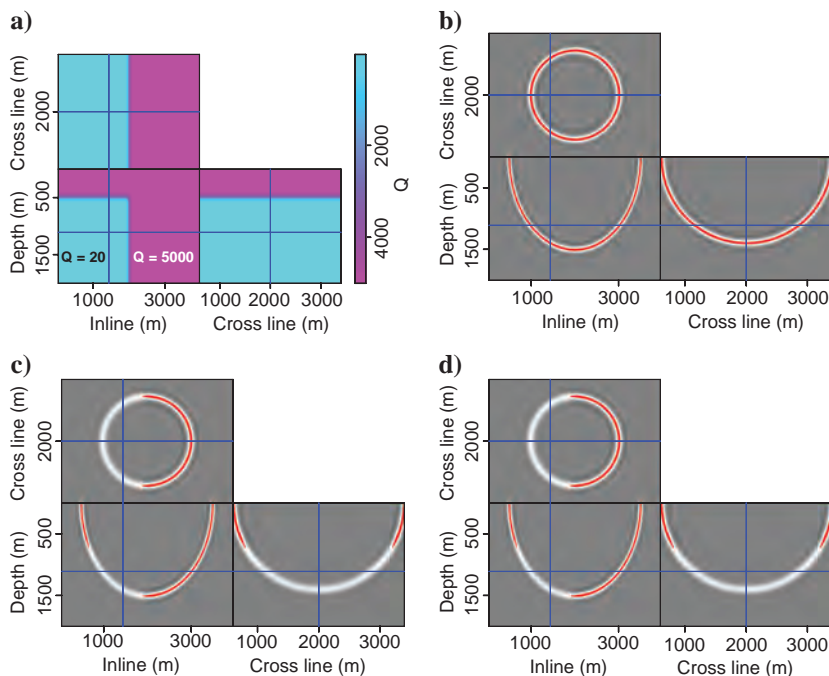


Figure 1. (a) A 3D heterogeneous Q model. The seismic attenuation is strong with $Q = 20$ in the lower left corner. The snapshots at 1 s are obtained from (b) the acoustic wave equation, (c) equation 4, and (d) equation 6. The red color indicates high amplitudes in these snapshots.

shown in Figure 1a. The Q model is actually a 2.5D step model with the step in the xy -plane and with no variation in the y -direction. The attenuation is strong in the lower left corner ($Q = 20$) whereas it can be ignored in the rest ($Q = 5000$). The model size is $3920 \times 2800 \times 2000$ m. An exploding source located at the center of model surface initializes wave propagation. The source is a Ricker wavelet with a center frequency of 18 Hz and a time sample of 4 ms. The Nyquist frequency of the source is therefore 125 Hz. Because seismic waves are band limited and this example is designed to simulate the wave propagation in a viscoacoustic model, it is not particularly significant how the Nyquist frequency is covered. For the purpose of this example, the Nyquist frequency of the source is replaced by a maximum frequency $f_{\max} = 37.5$ Hz, which is approximately twice the dominant frequency. In this example, we use the $O(2,2)$ finite-difference schemes on centered grids to solve the acoustic wave equation and equation 6 whereas we use a $O(2,2)$ finite-difference scheme on staggered grids to solve equation 4. According to Dablain (1986), the number of

points needed to cover the Nyquist frequency is eight for the $O(2,2)$ schemes. The weights of the second-order accurate finite-difference operator are 1, -2, and 1. The spatial sampling rates Δx , Δy , and Δz in the finite-difference scheme are therefore 5 m according to $\Delta x = v_{\min}/(n \times f_N)$ (Dablain, 1986). For a given reference frequency f_0 , the relaxation times can be converted from Q based on the τ - Q relationships (Carcione, 2001) as

$$\tau_\sigma = \frac{\sqrt{Q^2 + 1} - 1}{2\pi f_0 Q} \quad (14)$$

and

$$\tau_\epsilon = \frac{\sqrt{Q^2 + 1} + 1}{2\pi f_0 Q}. \quad (15)$$

In this example, the reference frequencies $f_0 = 18$ Hz and $Q_{\min} = 20$ yield $\tau_{\max} = 1.1051249$. Consequently, the time step in the finite-difference scheme must be equal to or less than 1.183 ms according to equation 12.

The 3D snapshots shown in Figure 1b–1d are obtained from the acoustic wave equation, equations 4 and 6, respectively. As expected equations 4 and 6 yield similar results because equation 6 is essentially another way to implement equation 4. Compared to the acoustic snapshot, the viscoacoustic snapshots clearly demonstrate the attenuation effects in the left part of the depth slice, in the lower left part of the inline section and in the deep part of the xline section.

A modified Marmousi model

The modified Marmousi model includes a water layer from the surface down to 500 m (Figure 2a, the water layer is not shown for simplicity). The model size is 9200×3500 m². For simplicity, density is set equal to 1 g/cm^3 . The Q model used in this example is shown in Figure 2b. The attenuation in water is essentially zero with a Q of 5000. Below the water layer, the relationship between Q and velocity v (in m/s) is $Q = 20 \times v/1500$. This relationship results in strong attenuation characteristic of shallow unconsolidated sediments near the seafloor (Hamilton, 1980). The strong attenuation in the shallow sediments makes the model more challenging for waveform inversion and will serve to demonstrate the thesis of this paper. We start waveform inversions with an initial velocity model shown in Figure 2c. In the starting model, the velocity v (in m/s) below the water layer is a linear function of depth z (in m)

$$v(z) = 1500 + 0.8333 \times (z - 500). \quad (16)$$

The application of waveform inversion starting from the poor initial velocity model is another challenge.

Two towed marine surveys are generated, the first being a purely acoustic data set and the second a viscoacoustic synthetic data set using the velocity model (Figure 2a) and the Q model (Figure 2b) with a flat spectrum source. The source is obtained by applying a first-order low-pass Butterworth filter with the cutoff frequency of 8.5 Hz to a spike. The relaxation times are obtained from the Q model at the reference frequency of 6 Hz according to equations 13 and 15. The surveys consist of 125 shots spaced every 100 m and

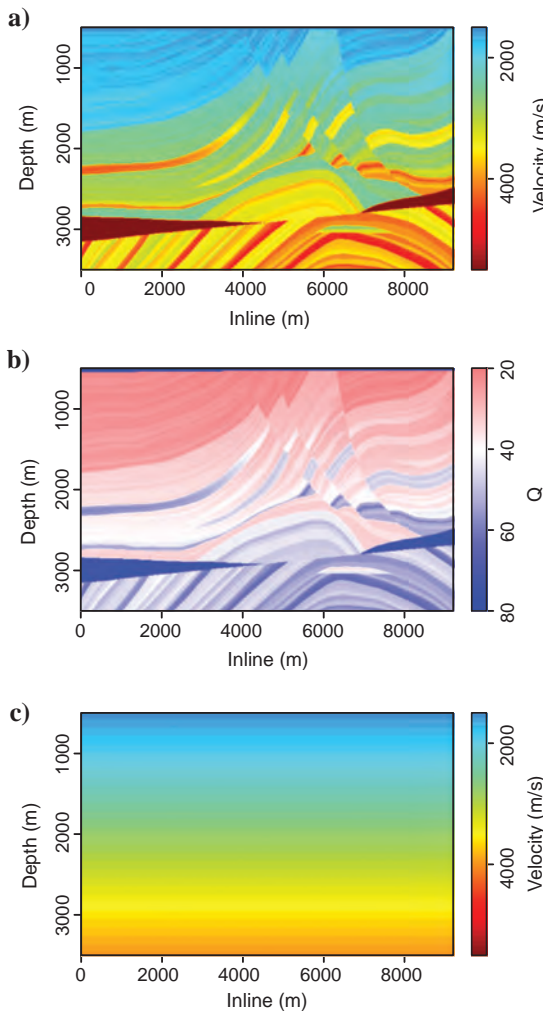


Figure 2. (a) A modified Marmousi velocity model that includes a water layer from surface down to 500 m. The water layer is not shown. (b) A Q model is obtained from the velocity model as described in the text. Q is 5000 in water. (c) The initial velocity model for waveform inversions.

located at the free surface. All the shots are recorded with 161 hydrophones spaced every 20 m on the free surface. The record length of the synthetic data is 4.2 s with the time step of 4 ms. The grid spacing of 10 m is chosen in the x - and z -directions, and the time sample rate is set equal to 0.00178 s for finite-difference solutions.

An acoustic shot gather is shown in Figure 3a and a viscoacoustic shot gather shown in Figure 3b. Their shots are located at 5100 m in the inline direction at the water surface. The Q model causes strong attenuation and dispersion, including amplitude attenuation and phase shift (Figure 4), in the viscoacoustic shot gathers. The attenuation effects increase with traveltimes because seismic waves take more oscillations along a longer path. Because viscoacoustic events propagate faster than acoustic events (Carcione et al., 1988a), they arrive earlier than their corresponding acoustic events.

In this study, a constant Q is approximated with a single SLS. The quality factor Q is given by (Carcione et al., 1988a)

$$M_c(\omega) = M_R \frac{1 + i\omega\tau_\epsilon}{1 + i\omega\tau_\sigma} \quad (17)$$

and

$$Q(\omega) = \frac{\text{Re}(M_c)}{\text{Im}(M_c)}, \quad (18)$$

where M_c is the complex bulk modulus; M_R is the acoustic or relaxed bulk modulus; and $M_R = \rho v^2$, where v is the acoustic velocity. Let us consider the approximation of $Q = 30$ between 0.5 and 20 Hz with a reference frequency of 6 Hz. The approximate values of Q are lower than 40 between 3 and 13.5 Hz. This indicates that the attenuation is strong at frequencies close to the reference frequency even for a low- Q value as in this example. Consequently, the frequency components close to the reference frequency in the viscoacoustic synthetic data are attenuated (Figure 5a). The amplitude spectrum shown in Figure 5b shows very weak attenuation effects. This spectrum is obtained from the dashed-line box shown in Figure 3a. The signals in the dashed-line box come from the seismic waves that mainly propagate in water and, as stated earlier, the attenuation in water can be ignored, which explains the weak attenuation effects in Figure 5b.

We apply acoustic and viscoacoustic waveform inversions to the two synthetic data sets with the initial velocity model shown in Figure 2c. Because the initial velocity model is far from the real model shown in Figure 2c, multiscale techniques (Bunks et al., 1995) are used to avoid local-minima and cycle-skipping problems at all scales.

The first strategy is to group frequencies into four groups of increasing frequency content and perform sequential inversions from the lower frequency group to the higher frequency group. The waveform inversions are performed in the frequency band from 0 to 12 Hz. High-cut filters with 0–0–1–3 Hz, 0–0–3–6 Hz, 0–0–6–9 Hz, and 0–0–9–12 Hz are applied to the source wavelet and seismic data sets. The schedule of frequencies fully uses the seismic data up to 9 Hz to fully exploit the nonlinearity of the problem: For lower frequencies, the method is more tolerant of velocity errors

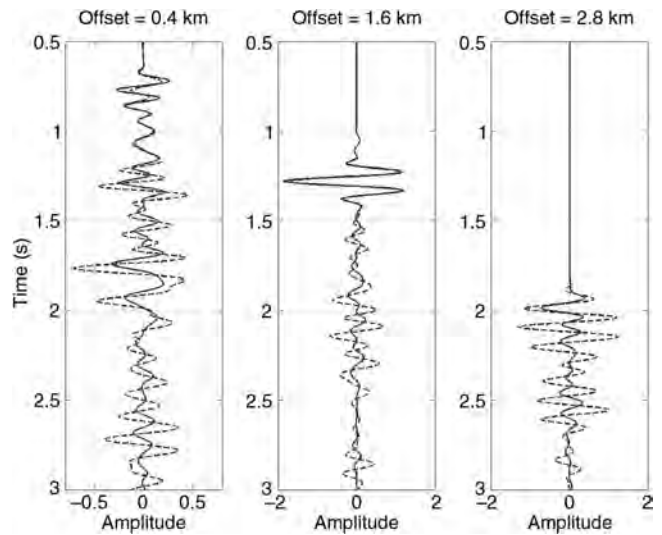


Figure 4. Seismic traces between 0.5 and 3 s at the offsets of 0.4, 1.6, and 2.8 km. The dashed line is obtained from the acoustic shot gather shown in Figure 3a, and the solid line from the viscoacoustic shot gather shown in Figure 3b. The attenuation dispersion includes amplitude attenuation and phase shift.

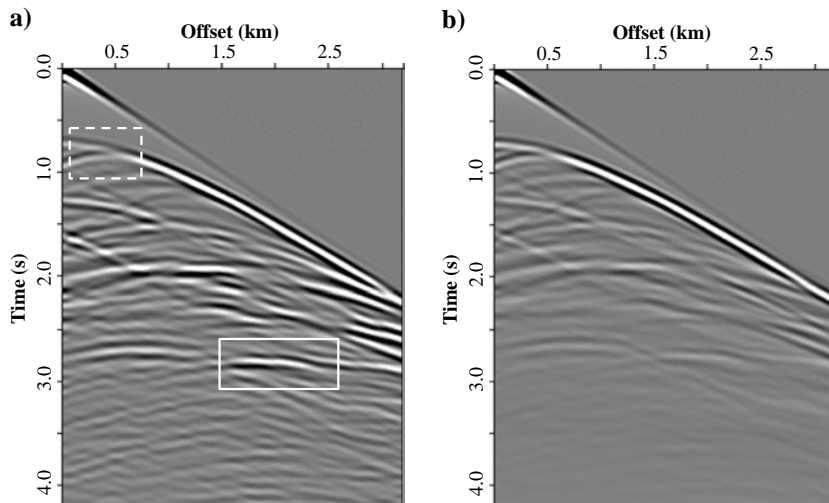


Figure 3. (a) An acoustic shot gather. (b) A viscoacoustic shot gather. They are clipped to the same absolute value. The dashed box shows an area where weak attenuation is expected, whereas a lot of attenuation effects are expected in the solid box as explained in the text.

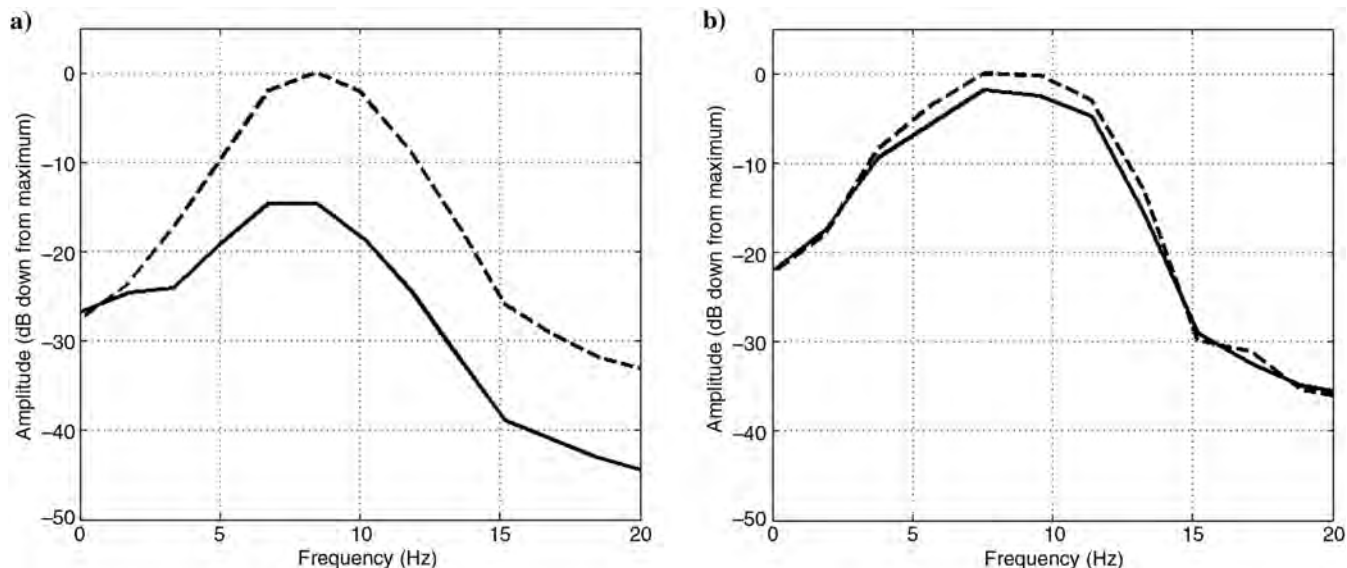


Figure 5. Amplitude spectra obtained from (a) the solid-line box and (b) the dashed-line box shown in Figure 3a. The dashed line is obtained from the acoustic shot gather shown in Figure 3a and the solid one from the viscoacoustic shot gather shown in Figure 3b.

because these are less likely to lead to errors of more than a half-cycle in the inversions. As the inversion proceeds, we move to progressively higher frequencies.

The second strategy is offset weighting. Inversion benefits from long-offset and transmission data to reconstruct the large and intermediate wavelengths of a model (Mora, 1987, 1988; Pratt and Worthington, 1990; Pratt, 1999). The offset weighting is helpful to separate reflected versus refracted energy and helps to strengthen the contribution of large-offset data. In this example, we use the $w(h)$ notation to describe the weight w at the offset h , where w is a linear function between two offsets. The offsets are grouped into four overlapping offset groups: $0(0)-0(2100)-1(2200)-1(3200)$, $0(0)-0(1000)-1(1100)-1(2100)-0(2200)-0(3200)$, $1(0)-1(1000)-0(1100)-0(3200)$, and $1(0)-1(3200)$. The offset groups are shown in Figure 6a. The schedule of offset weighting means that we use the large-offset data first and then move to progressively shorter offset data, and finally to the full-offset data.

The third strategy is to apply depth-dependent weights to gradients for velocity update (Shipp and Singh, 2002; Wang and Rao, 2009). The Marmousi model is a complex model with many thin layers and three faults. Compared to the shallow part with small velocity anomalies, the structure is more complex in the deeper part where a reservoir is located below 3000 m and high-velocity anomalies are located at the depth of 3000 m on the left side and at the depth of 2700 m on the right side. As a result, the deeper part of the model has large contributions to the total wavefield response. However, errors in shallow overburden invalidate the velocity update in the deeper part of the velocity model. To minimize this problem, we apply depth-dependent weights to gradients. In this paper, we use the (z, w) notation to describe the weight w at the depth z . The weights are a linear function between two depths. We use the following depth-dependent weights to develop a high-resolution velocity field in the deeper part: $(0,0)-(490,0)-(500,1)-(3500,1)$, $(0,0)-(1800,0)-(2000,1)-(3500,1)$, and $(0,0)-(490,0)-(500,1)-(3500,1)$. The two sets of depth-dependent weights

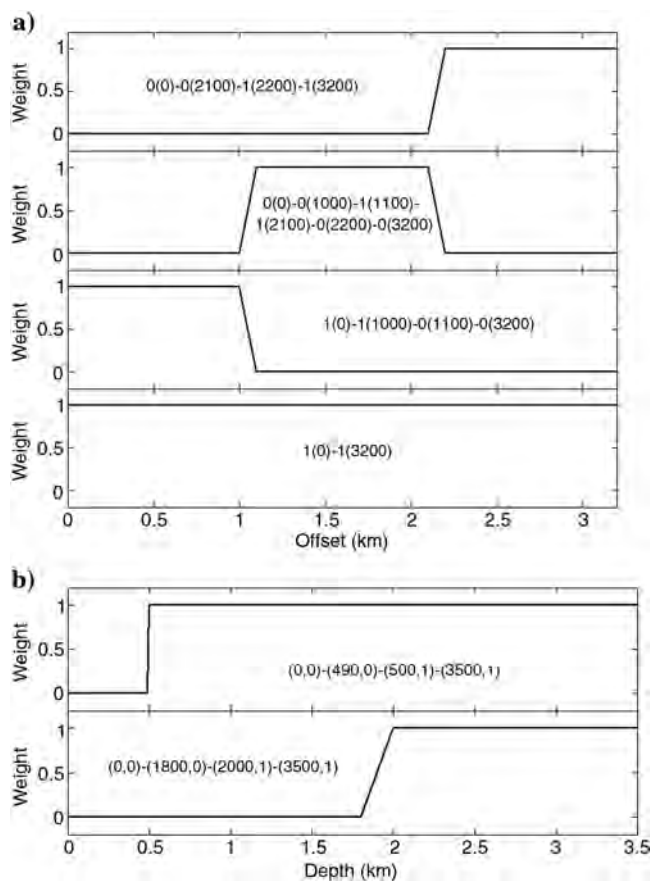


Figure 6. (a) The offset groups used in waveform inversions. The $w(h)$ notation describes the weight w at the offset h . (b) The depth-dependent weights applied to gradients. The (z, w) notation describes the weight w at the depth z .

are shown in Figure 6b. By using the depth-dependent weights, we update the whole model first, then the deep part, and then the whole model again.

We perform the inversions within the nested loops with the outer loop over the frequency groups, the middle loop over the offset weighting, and the inner loop over the depth-dependent weighting. For each combination of the strategies, eight iterations are carried out. As the inversion proceeds, the velocity model improves in the subsequent inversion. The same source wavelet is used in the inversion because it is used to generate the synthetic data sets. The Q model shown in Figure 2b is used in the viscoacoustic inversion.

The inverted velocity models are displayed in Figure 7 when the inversion is performed on the 0–0–1–3 Hz data. The low-frequency data yield the solutions of the longest scale component of the inversion problem. These inverted models are used to initialize the inversion problem with high-frequency components. The comparisons of Figure 7a versus Figure 7c and Figure 7b versus Figure 7d indicate that the choice of acoustic versus viscoacoustic waveform

inversion is not very significant if only very low frequencies are used.

The final inverted velocity models are displayed in Figure 8. When the acoustic waveform inversion is applied to the acoustic data set and the viscoacoustic waveform inversion is applied to the viscoacoustic data set, high-resolution velocity models shown in Figure 8a and 8d are produced. They are comparable to the true velocity model and reveal the geologic structures in details even in the deep section where the geologic structures are complex. The reservoir at 3000-m depth is clearly recovered in both inverted velocity models. We note the sharper resolution of the viscoacoustic inversion on the viscoacoustic data at all depths. The application of the acoustic inversion to the viscoacoustic data can still produce a reasonable inverted velocity model (Figure 8b). However, it lacks resolution because the high-frequency components are lost in the viscoacoustic data set and the attenuation effects are not compensated in the acoustic inversion. As a result, the reservoir is missed in the inverted model. When the viscoacoustic inversion is applied to

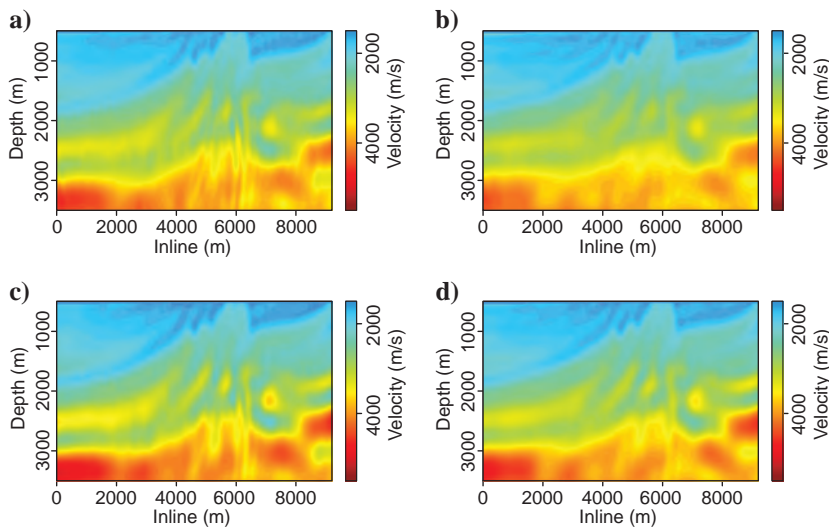


Figure 7. The inverted velocity models when the inversion is performed on the 0–0–1–3 Hz data. The acoustic waveform inversion is applied to the (a) acoustic and (b) viscoacoustic synthetic data. The viscoacoustic waveform inversion is applied to the (c) acoustic and (d) viscoacoustic synthetic data.

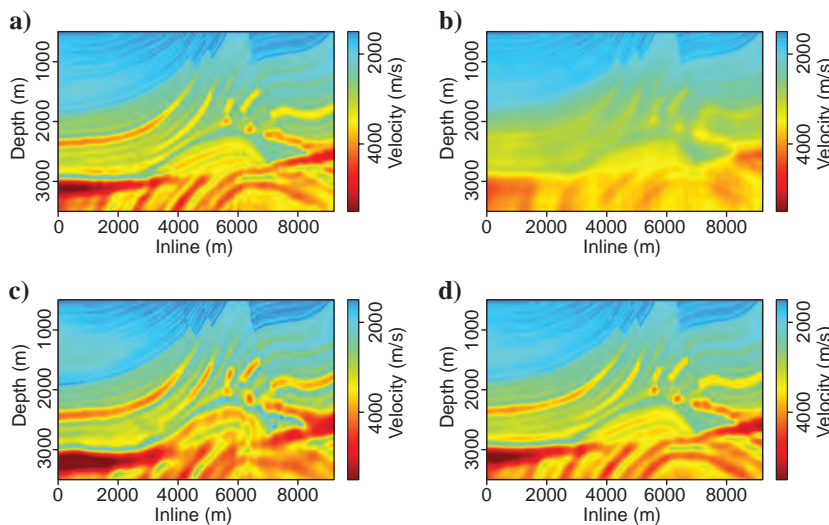


Figure 8. The final inverted velocity models. The acoustic waveform inversion is applied to the (a) acoustic and (b) viscoacoustic synthetic data. The viscoacoustic waveform inversion is applied to the (c) acoustic and (d) viscoacoustic synthetic data.

the acoustic data, the inverted model is shown in Figure 8c. Although the high-frequency components are included in the acoustic data, the kinematics of their propagation are wrong. This decreases the resolution with depth and produces incorrect inversion results in the deep section. The reservoir is not recovered either in the inverted model.

The vertical profiles from the center of the true model and the inverted models (Figure 7) obtained from the 0–0–1–3 Hz data are compared in Figure 9a. As discussed before, the attenuation is strong at frequencies close to the reference frequency (6 Hz) even

for low- Q values, the choice of acoustic versus viscoacoustic waveform inversion is not very significant for the low-frequency acoustic and viscoacoustic data. The vertical profiles from the center of the true model and the inverted models (Figure 8) obtained from the 0–0–9–12 Hz data are compared in Figure 9b. We note the large excursions of the velocity from the acoustic inversion on the viscoacoustic data and the great fidelity of the velocity from the viscoacoustic inversion of viscoacoustic data. Contrasted to Figure 9a, the high-frequency band emphasizes the effect of Q .

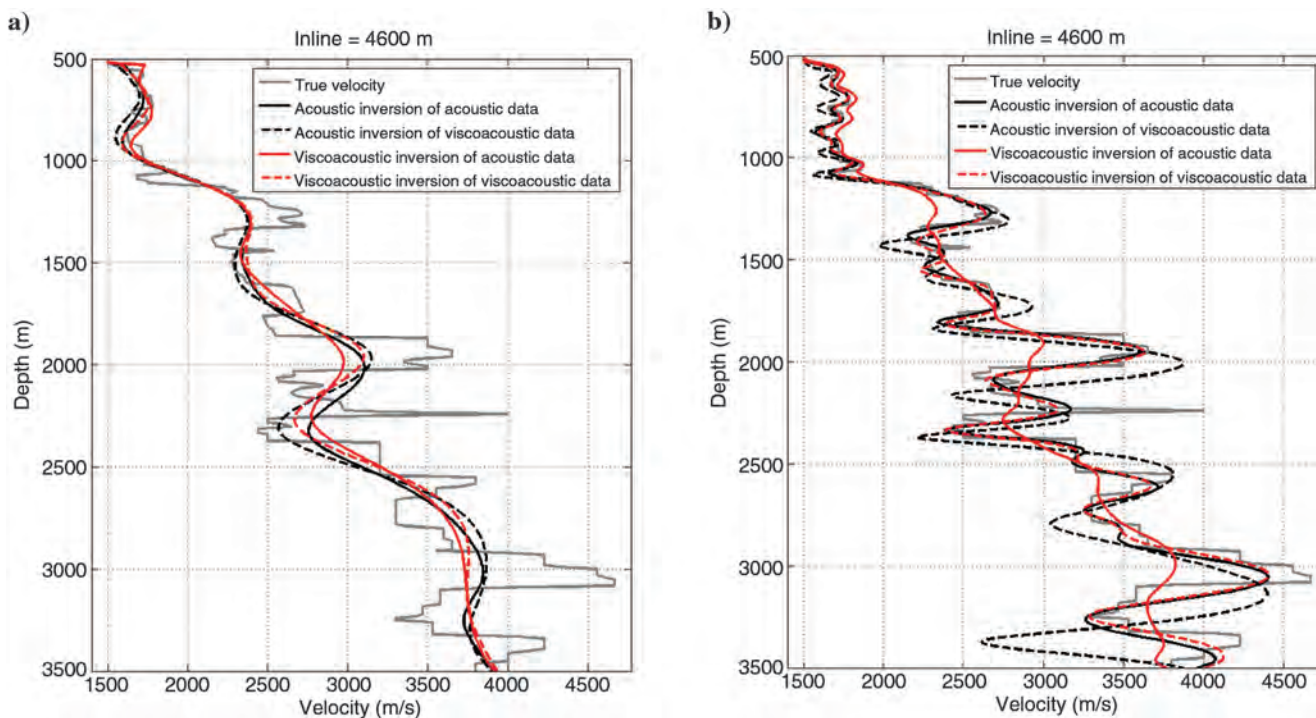
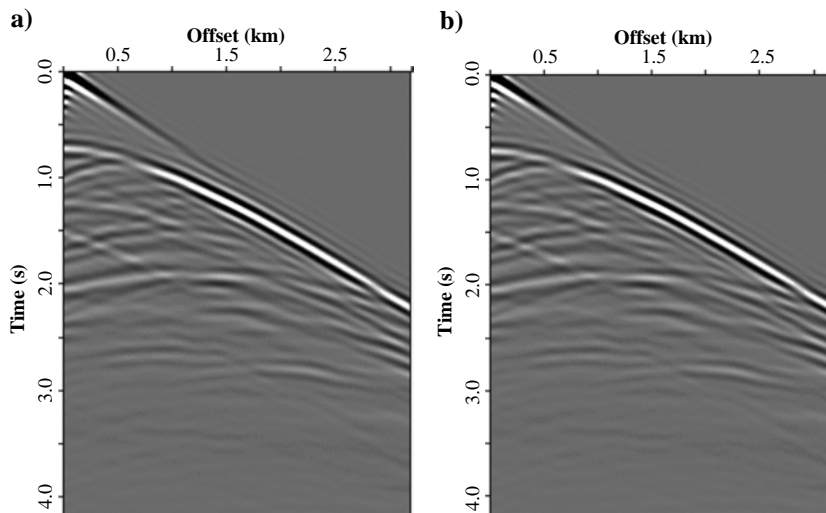


Figure 9. (a) Vertical profiles from the center of the true model and the inverted models (Figure 7) obtained from the 0–0–1–3 Hz data. (b) Vertical profiles from the center of the true model and the inverted models (Figure 8) obtained from the 0–0–9–12 Hz data.

Figure 10. (a) The acoustic shot gather shown in Figure 3a is filtered to 0–0–9–12 Hz. (b) The viscoacoustic shot gather shown in Figure 3b is filtered to 0–0–9–12 Hz.



The synthetic data shown in Figure 3 are filtered to 0–0–9–12 Hz, and the filtered data are displayed in Figure 10. The synthetic data obtained from the final inverted velocity models shown in Figure 8 and their residuals are displayed in Figures 11 and 12. The residuals are large when the acoustic inversion is applied to the viscoacoustic data, and the viscoacoustic inversion is applied to the acoustic data.

In the numerical example, all waveform inversions start from the poor initial velocity model (Figure 2c) without the large and intermediate wavelengths of the true velocity model (Figure 2a). The inverted models obtained from the 0–0–1–3 Hz data provide the large and intermediate wavelengths and act as the starting models for the high-frequency data. However, this is unattainable with field data recording because the low-frequency components are absent or are dominated by noises.

This numerical example illustrates that seismic attenuation can have large effects on waveform inversion. The attenuation effects should be compensated where strong attenuation is present. Choosing the most suitable inversion method for a particular seismic data set is important to get the most accurate velocity models of the subsurface.

GOM field data

The 3D ocean-bottom-cable (OBC) field data set was produced from a deep-water survey in the Green Canyon area of GOM. The survey has 19,901 shots located at an area of $20 \times 8 \text{ km}^2$. Each shot has 239 receivers. The water depth in the survey area is about 1000 m. A debubble filter was designed and applied to the prestack data set to compress wavelets by suppressing the air-gun bubble pulse. An f - k filter was applied to the prestack data set to remove high-amplitude noise spikes. Three-dimensional surface-related multiple elimination was applied.

We apply acoustic and viscoacoustic waveform inversions to the data set with receiver gathers. The waveform inversions are carried out in the frequency band of 2–3–8–9 Hz by using a source wavelet, which is estimated from the raw direct wave in the seismic data set. A starting velocity model shown in Figure 13a was obtained from ray-based tomography to initialize the inversions. Salt bodies are the main structures below 2200 m. In the inversions, the velocity model is kept constant in the water column and the salt bodies are masked so that the velocities of salt are also fixed. A layered velocity model down to 3000 m is generated from the average

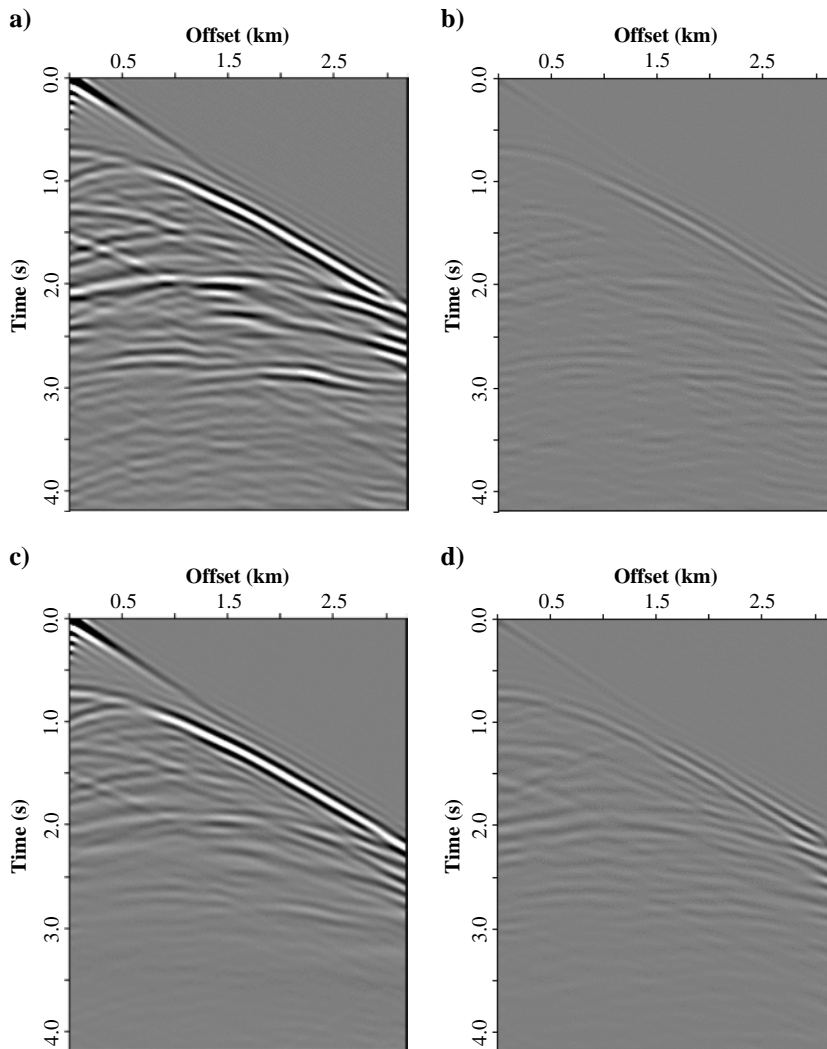


Figure 11. (a) The acoustic synthetic data obtained from the inverted velocity model shown in Figure 8a. The synthetic data are filtered to 0–0–9–12 Hz. (b) The residuals between the data (a) and the data shown in Figure 10a. (c) The acoustic synthetic data obtained from the inverted velocity model shown in Figure 8b. The synthetic data are filtered to 0–0–9–12 Hz. (d) The residuals between the data (c) and the data shown in Figure 10b.

Figure 12. (a) The viscoacoustic synthetic data obtained from the inverted velocity model shown in Figure 8c. The synthetic data are filtered to 0–0.9–12 Hz. (b) The residuals between the data (a) and the data shown in Figure 10a. (c) The viscoacoustic synthetic data obtained from the inverted velocity model shown in Figure 8d. The synthetic data are filtered to 0–0.9–12 Hz. (d) The residuals between the data (c) and the data shown in Figure 10b.

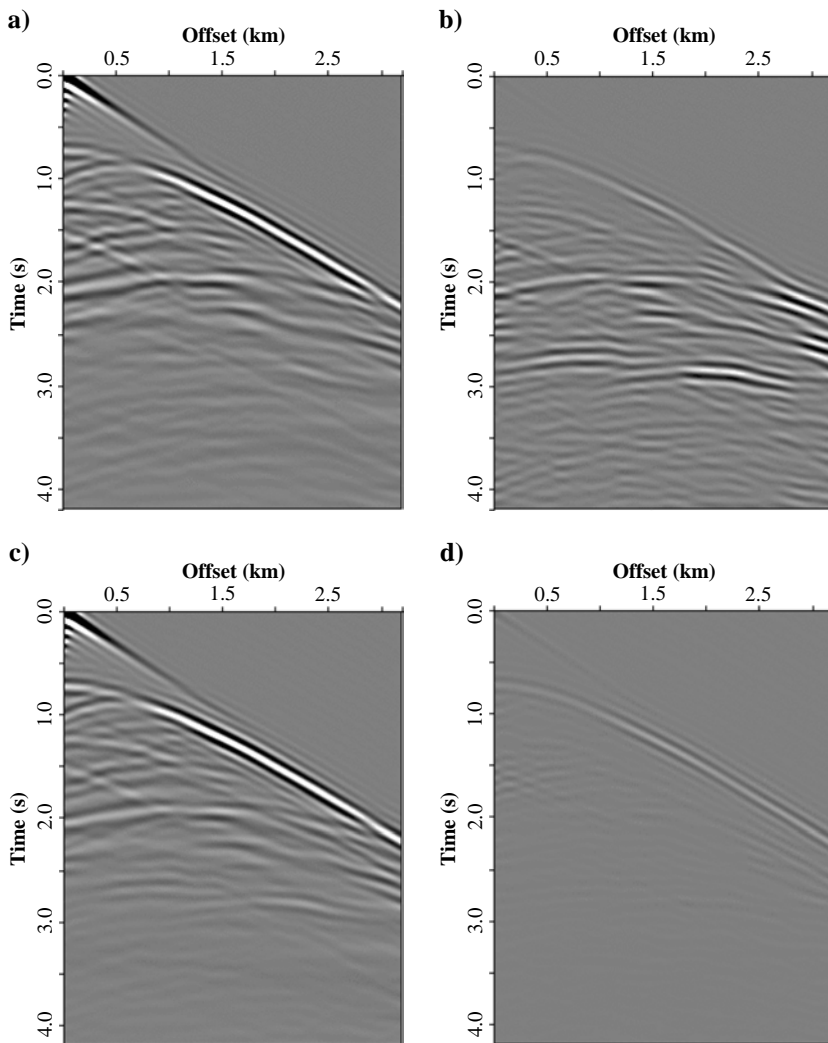
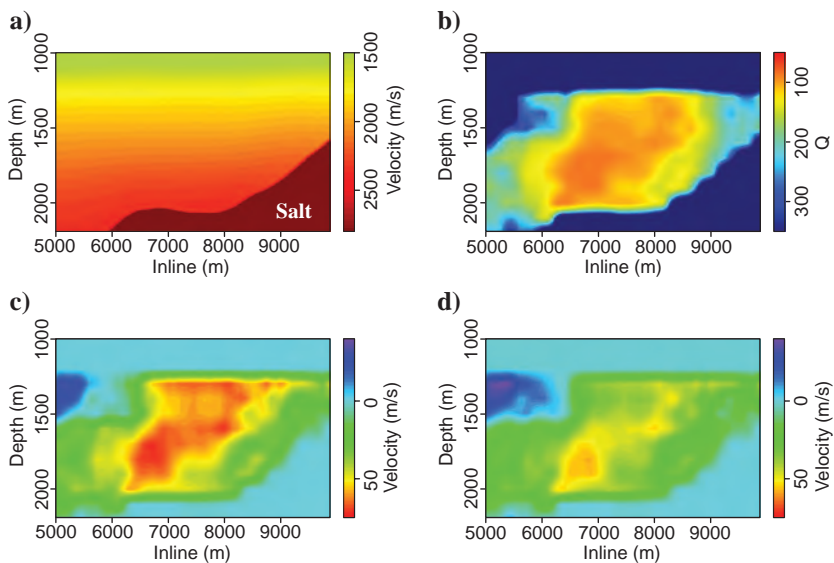


Figure 13. (a) Starting velocity model. (b) Inverted Q model. (c) The difference between the inverted velocity model obtained from acoustic inversion and the starting velocity model. (d) The difference between the inverted velocity model obtained from viscoacoustic inversion and the starting velocity model.



velocity at each depth of the starting velocity model. Ray tracing performed with the layered model indicates that diving energy turns at the depth of 2500 m and is observed at the offsets greater than 3000 m at the depth of 1000 m. To update the velocity between the water bottom and top salt, the seismic data in the offset range from 3000 to 7000 m are used in the inversions. This offset weighting is helpful to separate reflected versus refracted energy and, therefore, let us mainly focus on the diving waves to mitigate cycle-skipping artifacts in gradients. The cycle-skipping artifacts can be caused by near-offset reflected energy and far-offset diving energy (Virieux and Operto, 2009; Prioux et al., 2011). Gardner's equation (Gardner et al., 1974) is used to compute density from velocity for sediment, whereas the density of water is set equal to 1.03 g/cm³ and the density of salt is set equal to 2.175 g/cm³ (Bird et al., 2005).

Bai and Yingst (2013) use the forward and adjoint operators 6, 8, 9, and 11 to estimate a τ model by minimizing the objective function:

$$J(\tau) = \|d_0 - \alpha d\|_2^2. \quad (19)$$

The gradient for τ update is

$$g(\mathbf{x}) = -2\alpha \sum_{\mathbf{x}_s} \sum_t \left(\rho \nabla \cdot \frac{1}{\rho} \nabla P - \frac{1}{\tau} r \right) R, \quad (20)$$

where $P = P(\mathbf{x}, t; \mathbf{x}_s)$ is the predicted wavefield obtained from the forward modeling operators 6 and 8. The $R = R(\mathbf{x}, t; \mathbf{x}_s)$ is the wavefield obtained by applying the adjoint operators 9 and 11 on the residuals $(d_0 - \alpha d)$ with $\alpha = \langle d, d_0 \rangle / \|d\|^2$. A Q model is obtained from the inverted τ model based on equations 14 and 15:

$$Q = \sqrt{\left(\frac{2}{\tau} + 1\right)^2} - 1. \quad (21)$$

Given the reference frequency of 6 Hz, we first perform viscoacoustic waveform inversion to estimate a Q model starting from a constant $Q(=5000)$ model, using the source wavelet, the starting velocity model, and the density model mentioned above. In the waveform inversion, the starting velocity model is fixed. The inverted Q model is displayed in Figure 13b. The small values of $Q(\approx 90)$ mean relatively strong attenuation in the area.

Once the inverted Q model is obtained, acoustic and viscoacoustic waveform inversions are carried out to update the starting velocity model. Each waveform inversion performs 18 iterations. The inverted Q model is now kept fixed in the viscoacoustic inversion. The difference between the inverted velocity model obtained from the acoustic inversion and the starting velocity model is displayed in Figure 13c, whereas the difference between the inverted velocity model obtained from the viscoacoustic inversion and the starting velocity model is displayed in Figure 13d. It is noted that both inversions introduce an update with the low-wavenumber components. The updates mainly come from the refractions by offset-weighting receiver gathers. The velocity model obtained from the acoustic inversion is higher than the one obtained from the viscoacoustic inversion in the area with strong attenuation.

A receiver gather band-pass filtered of 2–3–8–9 Hz is displayed in Figure 14a. In Figure 14b, the receiver gather is offset weighted. In Figure 15, the field data in the box shown in Figure 14b are compared with the synthetic data obtained from the starting and inverted velocity models. Data-fitting benefits from the inversions as indicated by the ovals in the figure. Subtle difference in the solid ovals in Figure 15d, and Figure 15f indicates that the data fitting is slightly better by using the inverted velocity and Q models from the viscoacoustic inversion than the one by using the inverted velocity model from the acoustic inversion.

For quality control purposes, acoustic Kirchhoff depth migration is used for the acoustic case whereas viscoacoustic Kirchhoff depth migration is used for the viscoacoustic case. The attenuation effects are compensated in the viscoacoustic Kirchhoff migration. Figure 16a shows the image obtained from the starting velocity model without the benefit of incorporating any waveform inversion, indicating that energy is poorly focused in the area. The energy is much better focused in Figure 16b and 16c, which is obtained from the inverted models with and without attenuation, respectively. The image resolution is slightly improved by using the models determined with the viscoacoustic waveform inversion, as indicated in the ovals in these figures. A lot of events are not flattened at the far offset in the offset gathers obtained from the Kirchhoff migration with the starting velocity model (Figure 17a). They are improved by using

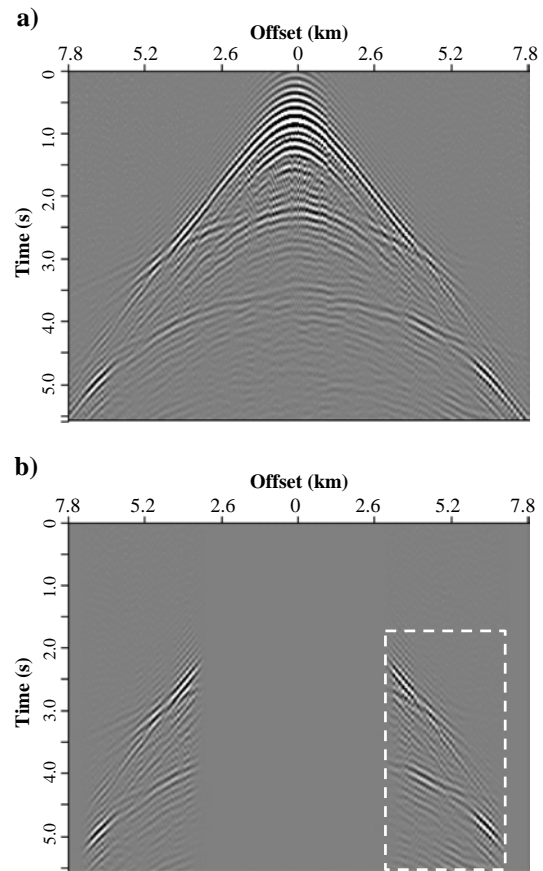


Figure 14. (a) A receiver gather is band-pass filtered of 2–3–8–9 Hz. (b) The receiver gather in (a) offset weighted between 3000 and 7000 m.

the inverted velocity model without Q compensation (Figure 17b). However, some events are slightly overcorrected, as highlighted in the ovals in the figure. This overcorrection is partially addressed by using the inverted models obtained with Q compensation (Figure 17c). The very last strong offset events come from the top of salt. Because the salt bodies are not updated, the last strong events are less flat as shown in Figure 17b and 17c. The offset ranges from 200 to 6000 m in these offset gathers.

It should be noted that we are using an iterative procedure, where we start with an initial velocity model (albeit a very good model in this example), from which we obtain a Q model through an inversion step, and then iterate. This procedure is consistent with the discussion by Tarantola (1988). In the field data set example that we

have shown, only a second velocity inversion was needed after the Q determination. This is because the starting velocity model was already very accurate.

CONCLUSIONS

In this paper, we have presented the theory of viscoacoustic waveform inversion in the time domain for velocity estimation. Viscoacoustic wave equations for forward modeling and their adjoint are derived to compensate for the seismic attenuation in viscoacoustic waveform inversion. We solve the equations by stable finite-difference schemes on centered grids with high-order accuracy to extrapolate seismic wavefields. Numerical examples demonstrate

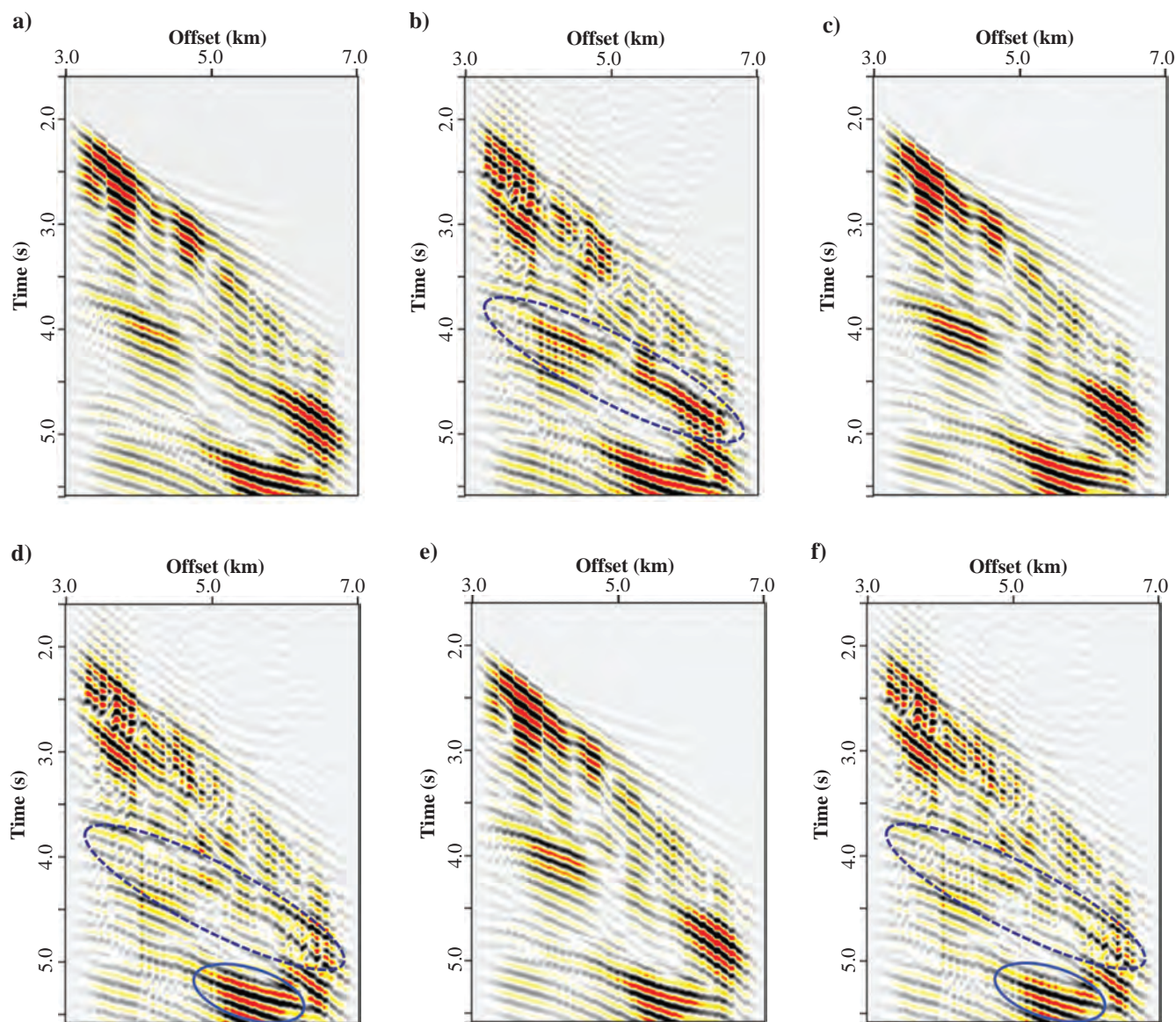


Figure 15. The field data in the box shown in Figure 10b are compared with synthetic data. (a) The synthetic data obtained from the starting velocity model. (b) The residuals between the field data and the panel (a). (c) The synthetic data obtained from the inverted velocity model from acoustic inversion. (d) The residuals between the field data and the panel (c). (e) The synthetic data obtained from the inverted velocity model from viscoacoustic inversion. (f) The residuals between the field data and the panel (e).

reasonable attenuative behaviors and thus indicate that the viscoacoustic equations can handle complex Q models.

The quality of waveform inversion depends on the adequacy of forward modeling and of its adjoint to describe the physics behind what we observe in nature. The tests presented in this paper indicate that the choice of the most suitable inversion method is important for a specific seismic data to produce the highest quality inversion results. The tests also illustrate that strong seismic attenuation can have significant effects on waveform inversion. The attenuation effects should be compensated otherwise they can reduce the resolution of inversion results or even cause inversion to produce incorrect results. The tests with the field data set indicate that the inverted

velocity models determined from the acoustic and viscoacoustic inversions are helpful to improve images and offset gathers obtained from migration. Compared to the acoustic inversion, the viscoacoustic inversion is a realistic approach for real earth materials because the attenuation effects are compensated.

ACKNOWLEDGMENTS

We thank ION Geophysical Corporation for the permission to publish this work. We thank our colleagues at ION Geophysical Corporation for helpful discussions, especially H. Jaramillo, C. Wang, G. Chen, M. Cvetkovic, H. Delome, P. Farmer, and J. Zhou. We especially thank M. Dolliazal for Q -Kirchhoff depth migration in the GOM field data example. Thanks go to IFP for the Marmousi model. We also thank several reviewers for excellent suggestions and comments. Finally, we are indebted to and thank M. Malinowski for insights into the various techniques and data issues that he encountered and excellent suggestions for improving this paper.

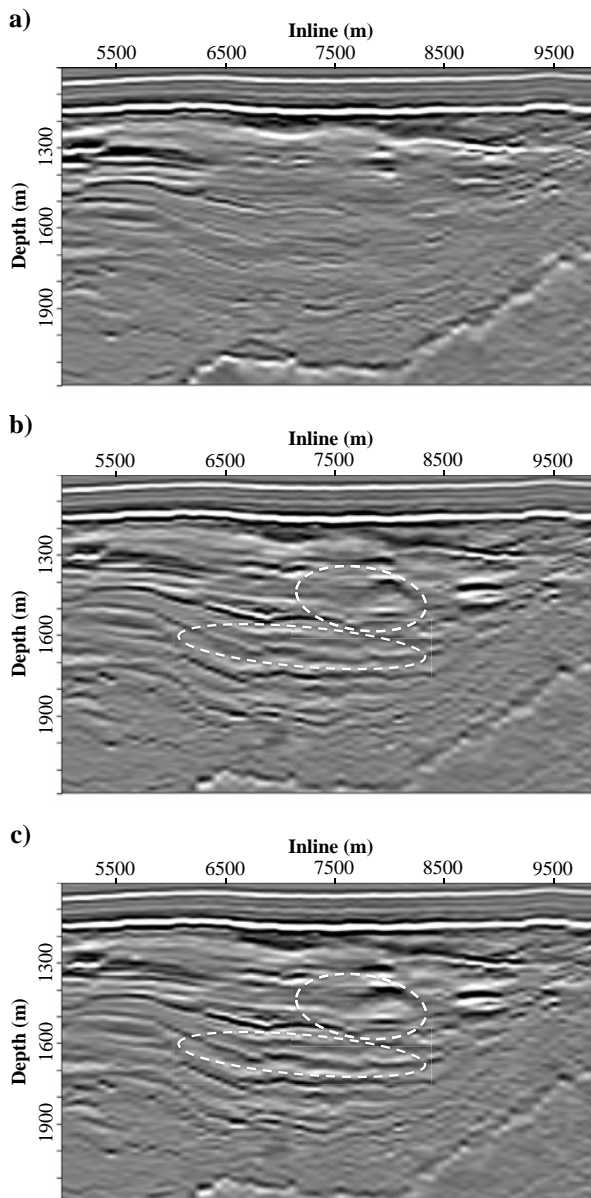


Figure 16. Migration images obtained from (a) the starting velocity model and the inverted velocity models obtained from the (b) acoustic and (c) viscoacoustic waveform inversions.

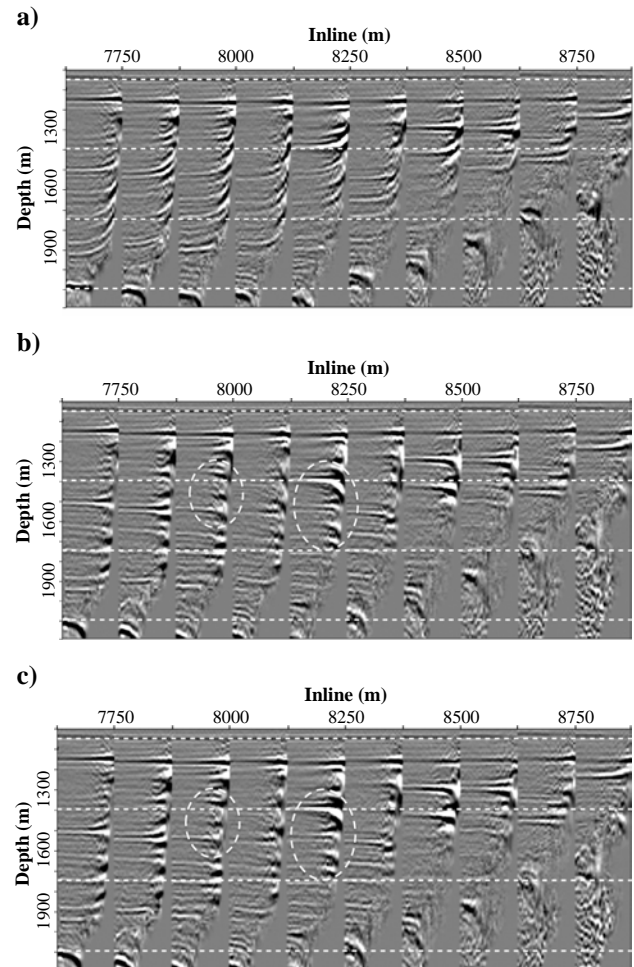


Figure 17. Offset gathers obtained from (a) the starting velocity model and the inverted velocity models obtained from the (b) acoustic and (c) viscoacoustic waveform inversions. In panel (c), over-corrected events in (b) are now flat.

APPENDIX A

DERIVATION OF FORWARD VISCOACOUSTIC WAVE EQUATION

Here, we show the derivation without the source term. Differentiating equation 4 in time gives

$$\frac{\partial^2 P}{\partial t^2} = - \frac{\partial \left[\kappa \left(1 + \tau e^{-\frac{t}{\tau_\sigma}} \right) H(t) \right]}{\partial t} * \nabla \cdot \frac{\partial \mathbf{v}}{\partial t}. \quad (\text{A-1})$$

Substituting equation 5 and the bulk modulus $\kappa(\mathbf{x}) = \rho(\mathbf{x})v(\mathbf{x})^2$ into equation A-1 reads

$$\frac{1}{v^2} \frac{\partial^2 P}{\partial t^2} = \frac{\partial G}{\partial t} * \left[\rho \nabla \cdot \left(\frac{1}{\rho} \nabla P \right) \right] \quad (\text{A-2})$$

with

$$G = \left(1 + \tau e^{-\frac{t}{\tau_\sigma}} \right) H(t). \quad (\text{A-3})$$

The relaxation function G determines the viscous behavior of the material. Differentiating equation A-3 in time yields

$$\frac{\partial G}{\partial t} = (1 + \tau) \delta(t) + \frac{\tau}{\tau_\sigma} e^{-\frac{t}{\tau_\sigma}} H(t), \quad (\text{A-4})$$

where $\delta(t)$ is the Dirac delta function. Substituting equation A-4 into A-2 results in the second-order differential equation 8 with the definition of the memory variable r in equation 7.

Differentiating equation 7 in time gives

$$\frac{\partial r}{\partial t} = \frac{\tau}{\tau_\sigma} \left\{ \rho \nabla \cdot \left(\frac{1}{\rho} \nabla P \right) - \frac{1}{\tau_\sigma} \left[e^{-\frac{t}{\tau_\sigma}} H(t) \right] * \left[\rho \nabla \cdot \left(\frac{1}{\rho} \nabla P \right) \right] \right\}. \quad (\text{A-5})$$

Combining equations 7 and A-5 leads to the first-order differential equation 8.

APPENDIX B

DERIVATION OF ADJOINT OPERATOR

Without the source term the forward modeling operator in equation 6 reads

$$\frac{1}{v^2} \frac{\partial^2 P}{\partial t^2} - (1 + \tau) \rho \nabla \cdot \frac{1}{\rho} \nabla P + \frac{\tau}{\tau_\sigma} e^{-\frac{t}{\tau_\sigma}} H(t) * \rho \nabla \cdot \frac{1}{\rho} \nabla P = 0. \quad (\text{B-1})$$

The adjoint T^* of an operator T has the property $\langle Tx, y \rangle = \langle x, T^*y \rangle$. This property results in

$$\begin{aligned} & \left\langle \frac{1}{v^2} \frac{\partial^2 P}{\partial t^2} - (1 + \tau) \rho \nabla \cdot \frac{1}{\rho} \nabla P + \frac{\tau}{\tau_\sigma} e^{-\frac{t}{\tau_\sigma}} H(t) * \rho \nabla \cdot \frac{1}{\rho} \nabla P, u \right\rangle \\ &= \left\langle P, \frac{1}{v^2} \frac{\partial^2 u}{\partial t^2} - \nabla \cdot \frac{1}{\rho} \nabla (1 + \tau) \rho u \right. \\ & \quad \left. + \nabla \cdot \frac{1}{\rho} \nabla \rho \left[\frac{\tau}{\tau_\sigma} e^{-\frac{t}{\tau_\sigma}} H(-t) * u \right] \right\rangle. \quad (\text{B-2}) \end{aligned}$$

So, the adjoint of forward modeling is the second-order differential equation 9 with the definition of the memory variable \tilde{r} in equation 10.

Differentiating equation 10 in time reads

$$\frac{\partial \tilde{r}}{\partial t} = \frac{\tau}{\tau_\sigma} \left[-P + \frac{1}{\tau_\sigma} e^{-\frac{t}{\tau_\sigma}} H(-t) * P \right]. \quad (\text{B-3})$$

Combining equations 10 and B-3 yields the first-order differential equation 11.

REFERENCES

- Bai, J., and D. Yingst, 2013, Q estimation through waveform inversion: 75th Annual International Conference and Exhibition, EAGE, Extended Abstracts, Th-10-01.
- Barzilai, J., and J. Borwein, 1988, Two-point step size gradient methods: *IMA Journal of Numerical Analysis*, **8**, 141–148, doi: [10.1093/imanum/8.1.141](https://doi.org/10.1093/imanum/8.1.141).
- Billette, F., and G. Lambaré, 1998, Velocity macro-model estimation from seismic reflection data by stereotomography: *Geophysical Journal International*, **135**, 671–690, doi: [10.1046/j.1365-246X.1998.00632.x](https://doi.org/10.1046/j.1365-246X.1998.00632.x).
- Bird, D. E., K. Burke, S. A. Hall, and J. F. Casey, 2005, Gulf of Mexico tectonic history: Hotspot tracks, crustal boundaries, and early salt distribution: *AAPG Bulletin*, **89**, 311–328, doi: [10.1306/10280404026](https://doi.org/10.1306/10280404026).
- Blanch, J. O., J. O. A. Robertsson, and W. W. Symes, 1995, Modeling of a constant Q : Methodology and algorithm for an efficient and optimally inexpensive viscoelastic technique: *Geophysics*, **60**, 176–184, doi: [10.1190/1.1443744](https://doi.org/10.1190/1.1443744).
- Brossier, R., S. Operto, and J. Virieux, 2009, Seismic imaging of complex onshore structures by 2D elastic frequency-domain full-waveform inversion: *Geophysics*, **74**, no. 6, WCC105–WCC118, doi: [10.1190/1.3215771](https://doi.org/10.1190/1.3215771).
- Bunks, C., F. Saleck, S. Zaleski, and G. Chavent, 1995, Multiscale seismic waveform inversion: *Geophysics*, **60**, 1457–1473, doi: [10.1190/1.1443880](https://doi.org/10.1190/1.1443880).
- Carcione, J., 1993, Seismic modeling in viscoelastic media: *Geophysics*, **58**, 110–120, doi: [10.1190/1.1443340](https://doi.org/10.1190/1.1443340).
- Carcione, J. M., 2001, Wave fields in real media: Wave propagation in anisotropic, anelastic and porous media: Elsevier Science Ltd.
- Carcione, J. M., D. Kosloff, and R. Kosloff, 1988b, Wave propagation simulation in a linear viscoacoustic medium: *Geophysical Journal*, **93**, 393–401, doi: [10.1111/j.1365-246X.1988.tb02010.x](https://doi.org/10.1111/j.1365-246X.1988.tb02010.x).
- Carcione, J. M., D. Kosloff, and R. Kosloff, 1988a, Viscoacoustic wave propagation simulation in the earth: *Geophysics*, **53**, 769–777, doi: [10.1190/1.1442512](https://doi.org/10.1190/1.1442512).
- Charney, J. G., R. Fjörtoft, and J. von Neumann, 1950, Numerical integration of the barotropic vorticity equation: *Tellus*, **2**, 237–254, doi: [10.1111/j.2153-3490.1950.tb00336.x](https://doi.org/10.1111/j.2153-3490.1950.tb00336.x).
- Crank, J., and P. Nicolson, 1947, A practical method for numerical evaluation of solutions of partial differential equations of the heat conduction type: *Proceedings of the Cambridge Philosophical Society*, **43**, 50–67, doi: [10.1017/S0305004100023197](https://doi.org/10.1017/S0305004100023197).
- Dablain, M. A., 1986, The application of high-order differencing to the scalar wave equation: *Geophysics*, **51**, 54–66, doi: [10.1190/1.1442040](https://doi.org/10.1190/1.1442040).
- Day, S. M., and J. B. Minster, 1984, Numerical simulation of attenuated wavefields using a Padé approximant method: *Geophysical Journal of the Royal Astronomical Society*, **78**, 105–118, doi: [10.1111/j.1365-246X.1984.tb06474.x](https://doi.org/10.1111/j.1365-246X.1984.tb06474.x).
- Futterman, W. I., 1962, Dispersive body waves: *Journal of Geophysical Research*, **67**, 5279–5291, doi: [10.1029/JZ067i013p05279](https://doi.org/10.1029/JZ067i013p05279).
- Gardner, G. H. F., L. W. Gardner, and A. R. Gregory, 1974, Formation velocity and density — The diagnostic basics for stratigraphic traps: *Geophysics*, **39**, 770–780, doi: [10.1190/1.1440465](https://doi.org/10.1190/1.1440465).

- Gauthier, O., J. Virieux, and A. Tarantola, 1986, Two-dimensional nonlinear inversion of seismic waveforms: Numerical results: *Geophysics*, **51**, 1387–1403, doi: [10.1190/1.1442188](https://doi.org/10.1190/1.1442188).
- Gholami, Y., R. Brossier, S. Operto, A. Ribodetti, and J. Virieux, 2011, Acoustic VTI full waveform inversion: Sensitivity analysis and realistic synthetic examples: 81st Annual International Meeting, SEG, Expanded Abstracts, 2465–2470.
- Gholami, Y., R. Brossier, S. Operto, A. Ribodetti, J. Virieux, O. I. Barkved, and J. H. Kommedal, 2012, 2D multi-parameter VTI acoustic full waveform inversion of wide-aperture OBC data from the Valhall Field: 74th Annual International Conference and Exhibition, EAGE, Extended Abstracts, W032.
- Guittou, A., G. Ayeni, and E. Díaz, 2012, Constrained full-waveform inversion by model reparameterization: *Geophysics*, **77**, no. 2, R117–R127, doi: [10.1190/geo2011-0196.1](https://doi.org/10.1190/geo2011-0196.1).
- Hamilton, E. L., 1980, Geoacoustic modeling of the seafloor: *Journal of the Acoustical Society of America*, **68**, 1313–1340, doi: [10.1121/1.385100](https://doi.org/10.1121/1.385100).
- Higdon, R. L., 1991, Absorbing boundary conditions for elastic waves: *Geophysics*, **56**, 231–241, doi: [10.1190/1.1443035](https://doi.org/10.1190/1.1443035).
- Kamei, R., and R. G. Pratt, 2013, Inversion strategies for visco-acoustic waveform inversion: *Geophysical Journal International*, **194**, 859–884, doi: [10.1093/gji/ggt109](https://doi.org/10.1093/gji/ggt109).
- Kjartansson, E., 1993, Constant Q -wave propagation and attenuation: *Geophysical Prospecting*, **84**, 4737–4748, doi: [10.1029/JB084iB09p04737](https://doi.org/10.1029/JB084iB09p04737).
- Kolsky, H., 1956, The propagation of stress pulses in viscoelastic solids: *Philosophical Magazine*, **1**, no. 8, 693–710, doi: [10.1080/14786435608238144](https://doi.org/10.1080/14786435608238144).
- Lailly, P., 1983, The seismic inverse problem as a sequence of before stack migrations, in J. B. Bednar, R. Redner, E. Robinson, and A. Weglein, eds., *Conference on inverse scattering: Theory and applications*: SIAM206–220.
- Larsen, S., and J. Grieger, 1998, Elastic modeling initiative, Part III: 3-D computational modeling: 68th Annual International Meeting, SEG, Expanded Abstracts, 1803–1806.
- Lee, H.-Y., J. M. Koo, D.-J. Min, B. Kwon, and H.-S. Yoo, 2010, Frequency-domain elastic full waveform inversion for VTI media: *Geophysical Journal International*, **183**, 884–904, doi: [10.1111/j.1365-246X.2010.04767.x](https://doi.org/10.1111/j.1365-246X.2010.04767.x).
- Li, C., 2011, Compressive sensing for 3D data processing — A unified method and its applications: Ph.D. thesis, CAAM, Rice University.
- Liao, Q., and G. A. McMechan, 1996, Multifrequency viscoacoustic modeling and inversion: *Geophysics*, **61**, 1371–1378, doi: [10.1190/1.1444060](https://doi.org/10.1190/1.1444060).
- Liu, H.-P., D. L. Anderson, and H. Kanamori, 1976, Velocity dispersion due to anelasticity: Implications for seismology and mantle composition: *Geophysical Journal of the Royal Astronomical Society*, **47**, 41–58, doi: [10.1111/j.1365-246X.1976.tb01261.x](https://doi.org/10.1111/j.1365-246X.1976.tb01261.x).
- Ma, Y., D. Hale, B. Gong, and Z. J. Meng, 2012, Image-guided sparse-model full waveform inversion: *Geophysics*, **77**, no. 4, R189–R198, doi: [10.1190/geo2011-0395.1](https://doi.org/10.1190/geo2011-0395.1).
- Malinowski, M., S. Operto, and A. Ribodetti, 2011, High-resolution seismic attenuation imaging from wide-aperture onshore data by visco-acoustic frequency-domain full-waveform inversion: *Geophysical Journal International*, **186**, 1179–1204, doi: [10.1111/j.1365-246X.2011.05098.x](https://doi.org/10.1111/j.1365-246X.2011.05098.x).
- Mora, P., 1987, Nonlinear two-dimensional elastic inversion of multioffset seismic data: *Geophysics*, **52**, 1211–1228, doi: [10.1190/1.1442384](https://doi.org/10.1190/1.1442384).
- Mora, P., 1988, Elastic wave-field inversion of reflection and transmission data: *Geophysics*, **53**, 750–759, doi: [10.1190/1.1442510](https://doi.org/10.1190/1.1442510).
- Nemeth, T., E. Normark, and F. Qin, 1997, Dynamic smoothing in crosswell traveltimes tomography: *Geophysics*, **62**, 168–176, doi: [10.1190/1.1444115](https://doi.org/10.1190/1.1444115).
- Oh, J.-W., D.-J. Min, and F. J. Herrmann, 2012, Frequency-domain elastic waveform inversion using weighting factors related to source-deconvolved residuals: 74th Annual International Conference and Exhibition, EAGE, Extended Abstracts, W025.
- Operto, S., J. Virieux, P. Amestoy, J. L'Excellent, L. Giraud, and H. Ali, 2007, 3D finite-difference frequency-domain modeling of visco-acoustic wave propagation using a massively parallel direct solver: A feasibility study: *Geophysics*, **72**, no. 5, SM195–SM211, doi: [10.1190/1.2759835](https://doi.org/10.1190/1.2759835).
- Operto, S., J. Virieux, A. Ribodetti, and J. Anderson, 2009, Finite-difference frequencydomain modeling of viscoacoustic wave propagation in 2D tilted transversely isotropic (TTI) media: *Geophysics*, **74**, no. 5, T75–T95, doi: [10.1190/1.3157243](https://doi.org/10.1190/1.3157243).
- Plessix, R.-E., 2006, A review of the adjoint-state method for computing the gradient of a functional with geophysical applications: *Geophysical Journal International*, **167**, 495–503, doi: [10.1111/j.1365-246X.2006.02978.x](https://doi.org/10.1111/j.1365-246X.2006.02978.x).
- Plessix, R.-E., and H. Rynja, 2010, VTI full waveform inversion: A parameterization study with a narrow azimuth streamer data example: 80th Annual International Meeting, SEG, Expanded Abstracts, 962–966.
- Pratt, R. G., 1999, Seismic waveform inversion in the frequency domain, Part 1: Theory and verification in a physical scale model: *Geophysics*, **64**, 888–901, doi: [10.1190/1.1444597](https://doi.org/10.1190/1.1444597).
- Pratt, R. G., and M. H. Worthington, 1990, Inverse theory applied to multi-source crosshole tomography. Part 1: Acoustic wave-equation method: *Geophysical Prospecting*, **38**, 287–310, doi: [10.1111/j.1365-2478.1990.tb01846.x](https://doi.org/10.1111/j.1365-2478.1990.tb01846.x).
- Prieux, V., R. Brossier, Y. Gholami, S. Operto, J. Virieux, O. I. Barkved, and J. H. Kommedal, 2011, On the footprint of anisotropy on isotropic full waveform inversion: The Valhall case study: *Geophysical Journal International*, **187**, 1495–1515, doi: [10.1111/j.1365-246X.2011.05209.x](https://doi.org/10.1111/j.1365-246X.2011.05209.x).
- Robertsson, J. O. A., J. O. Blanch, and W. W. Symes, 1994, Viscoelastic finite-difference modeling: *Geophysics*, **59**, 1444–1456, doi: [10.1190/1.1443701](https://doi.org/10.1190/1.1443701).
- Sears, T. J., P. J. Barton, and S. C. Singh, 2010, Elastic full waveform inversion of multicomponent ocean-bottom cable seismic data: Application to Alba Field, UK, North Sea: *Geophysics*, **75**, no. 6, R109–R119, doi: [10.1190/1.3484097](https://doi.org/10.1190/1.3484097).
- Sears, T. J., S. C. Singh, and P. J. Barton, 2008, Elastic full waveform inversion of multicomponent OBC seismic data: *Geophysical Prospecting*, **56**, 843–862, doi: [10.1111/j.1365-2478.2008.00692.x](https://doi.org/10.1111/j.1365-2478.2008.00692.x).
- Shen, P., W. W. Symes, and C. Stolk, 2003, Differential semblance velocity analysis by wave-equation migration: 73rd Annual International Meeting, SEG, Expanded Abstracts, 2132–2135.
- Shin, C., and D.-J. Min, 2006, Waveform inversion using a logarithmic wavefield: *Geophysics*, **71**, no. 3, R31–R42, doi: [10.1190/1.2194523](https://doi.org/10.1190/1.2194523).
- Shipp, R. M., and S. C. Singh, 2002, Two-dimensional full wavefield inversion of wide-aperture seismic streamer data: *Geophysical Journal International*, **151**, 325–344, doi: [10.1046/j.1365-246X.2002.01645.x](https://doi.org/10.1046/j.1365-246X.2002.01645.x).
- Sirgue, L., O. I. Barkved, J. P. V. Gestel, O. J. Askim, and J. H. Kommedal, 2009, 3D waveform inversion on Valhall wide-azimuth OBC: 71st Annual International Conference and Exhibition, EAGE, Extended Abstracts, U038.
- Sirgue, L., and R. G. Pratt, 2004, Efficient waveform inversion and imaging: A strategy for selecting temporal frequencies: *Geophysics*, **69**, 231–248, doi: [10.1190/1.1649391](https://doi.org/10.1190/1.1649391).
- Smithyman, B. R., and R. M. Clowes, 2013, Waveform tomography in 2.5D: Parameterization for crooked-line acquisition geometry: *Journal of Geophysical Research: Solid Earth*, **118**, 2119–2135, doi: [10.1002/jgrd.50222](https://doi.org/10.1002/jgrd.50222).
- Symes, W. W., and J. J. Carazzone, 1991, Velocity inversion by differential semblance optimization: *Geophysics*, **56**, 654–663, doi: [10.1190/1.1443082](https://doi.org/10.1190/1.1443082).
- Tarantola, A., 1984, Inversion of seismic reflection data in the acoustic approximation: *Geophysics*, **49**, 1259–1266, doi: [10.1190/1.1441754](https://doi.org/10.1190/1.1441754).
- Tarantola, A., 1986, A strategy for nonlinear elastic inversion of seismic reflection data: *Geophysics*, **51**, 1893–1903, doi: [10.1190/1.1442046](https://doi.org/10.1190/1.1442046).
- Tarantola, A., 1987, Inverse problem theory: Methods for data fitting and model parameter estimation: Elsevier.
- Tarantola, A., 1988, Theoretical background for the inversion of seismic waveforms, including elasticity and attenuation: *Pure and Applied Geophysics*, **128**, 365–399, doi: [10.1007/BF01772605](https://doi.org/10.1007/BF01772605).
- Toksöz, M. N., and D. H. Johnston, 1981, Seismic wave attenuation: SEG.
- Vigh, D., J. Kapoor, and H. Li, 2011, Full-waveform inversion application in different geological settings: 81st Annual International Meeting, SEG, Expanded Abstracts, 2374–2378.
- Vigh, D., and E. W. Starr, 2008, 3D prestack plane-wave, full-waveform inversion: *Geophysics*, **73**, no. 5, VE135–VE144, doi: [10.1190/1.2952623](https://doi.org/10.1190/1.2952623).
- Virieux, J., and S. Operto, 2009, An overview of full-waveform inversion in exploration geophysics: *Geophysics*, **94**, no. 6, WCC127–WCC152, doi: [10.1190/1.3238367](https://doi.org/10.1190/1.3238367).
- Wang, C., D. Yingst, R. Bloor, and J. Leveille, 2012, Application of VTI waveform inversion with regularization and preconditioning to real 3D data: 74th Annual International Conference and Exhibition, EAGE, Extended Abstracts, W009.
- Wang, Y., and Y. Rao, 2009, Reflection seismic waveform tomography: *Journal of Geophysical Research*, **114**, B03304, doi: [10.1029/2008JB005916](https://doi.org/10.1029/2008JB005916).
- Yingst, D., C. Wang, J. Park, R. Bloor, J. P. Leveille, and P. Farmer, 2011, Application of time domain and single-frequency waveform inversion to real data: 73rd Annual International Conference and Exhibition, EAGE, Extended Abstracts, F031.